Development of skeletal kerosene mechanisms and application to supersonic combustion

Wei Yao, Kun Wu, and Xuejun Fan

Just Accepted

Development of skeletal kerosene mechanisms and

application to supersonic combustion

Wei Yao[1]   Kun Wu[2]   and   Xuejun Fan[3]

Key Laboratory of High-Temperature Gas Dynamics, Institute of Mechanics, CAS, Beijing 100190, China

School of Engineering Science, University of Chinese Academy of Science, Beijing 100049, China

Small-size kerosene mechanisms suitable for supersonic combustion modelings are generally scarce in the literature. This study presents five sets of skeletal kerosene mechanisms, respectively with 89 species/668 reactions (abbreviated as 89s/668r), 48s/197r, 39s/153r, 28s/92r and 19s/54r, together with validations in both ideal reactors and a realistic scramjet combustor. As the base level of fidelity validation, the adiabatic flame temperature, accumulated heat release, ignition delay, laminar flame speed, and time evolution behaviors agree reasonably with those predicted by the original detailed mechanism (2185s/8217r) over the initial temperatures ranging from 1200 to 2400 K and equivalence ratios from 0.7 to 1.5, which are the typical combustion conditions in scramjet combustors. The skeletal mechanisms are further validated in a three-dimensional full-combustor modeling employing Improved Delayed Detached Eddy Simulation (IDDES) together with the finite-rate Partially Stirred Reactor (PaSR) combustion model. As the second and third levels of fidelity validation, The mean flow fields, combustor efficiencies, intermediate species and turbulence-chemistry interaction modes predicted by the different skeletal mechanisms are compared and analyzed.

---

[1] Associate Professor, Institute of Mechanics (CAS), weiyao@imech.ac.cn.
[2] PHD student, Institute of Mechanics (CAS), wukun@imech.ac.cn.
[3] Professor, Institute of Mechanics (CAS), xfan@imech.ac.cn (Corresponding author).

I. Introduction

One of the main challenges in the modeling of hydrocarbon-fueled scramjet combustor originates from the ultra-large chemical mechanisms and the chemical stiffness. The species number and reaction steps increase with the molecule size roughly in an exponential trend [1]. Typically, the detailed mechanisms for small-molecule fuels (C_1- and C_2- based) consist of less than one hundred species, while large-molecule Jet fuels ($C_{>10}$-based) consist of hundreds of or even thousands of species. Kerosene as compound hydrocarbon fuel usually contains thousands of species, most in the molecular formula of $C_7 - C_{16}$ [2]. To simplify the chemical kinetic analysis, chemical surrogates are frequently used to simulate the complex multi-component hydrocarbon fuel. Even so, the detailed mechanisms developed based on surrogate species for kerosene-type fuels still contain thousands of elementary reactions [3, 4]. Although some detailed mechanisms for kerosene-type fuels (e.g., Jet-A, JP-8) have been developed [3-9], they are generally too large for three-dimensional (3-D) modeling without substantial reduction [1]. Indeed the computation using such detailed kerosene mechanisms is time-consuming even for zero-dimensional (0-D) modelings. The sizes of those detailed mechanisms are still growing with time due to new chemical kinetics are continuously discovered [1]. In addition to the large size, the dramatic differences in chemical time scales give rise to severe chemical stiffness. The oxidation of fast depleting radicals (e.g., H, OH, and CH) in the detailed mechanisms have much shorter reaction process than the pyrolysis of large fuel molecules (e.g., $C_{10}H_{22}$). The large chemical stiffness will significantly increase the computational cost by requiring a stricter time step in resolving the chemistry. For those, current supersonic combustion modelings are mostly based on hydrogen fuel (e.g., [10, 11]) and only a small portion of them are based on small-molecule hydrocarbon fuels (e.g., ethylene [12], methane [13] and acetone [14]). The pioneer studies of kerosene-fueled supersonic combustion are possibly those by Kumaran et al. [15, 16] and Zhang et al. [17, 18], where the complex chemistry is simulated by using global or semi-kinetic kerosene mechanisms [19-22].

Since the computational cost is scaled with the square of the species number [1], special efforts have been devoted to reducing the species number involved in the chemical mechanisms for kerosene combustion. The elimination of unimportant intermediate species and simplification of interconnected reaction chains can also effectively reduce the stiffness of the detailed mechanisms. In the serial studies conducted by the authors' group, the detailed kerosene mechanism proposed by Dagaut et al. [3] is reduced under the typical working condition range of scramjet combustors, i.e., equivalence ratio of 0.7-1.5, static pressure of 0.5-3.0 bar, and static temperature of 300-3000 K. In those mechanisms, kerosene is surrogated by three components: 28.8% iso-octane, 62.4% n-decane, 8.8% n-

propylcyclohexane in mass fraction. Till now, five versions of skeletal mechanisms, respectively 89s/668r

[23], 39s/153r [24], 28s/92r [25] and 19s/54r [26], have been developed from the original 2815s/8217r mechanism [3] by using a

highly efficient and reliable Directed Relation Graph with Error Propagation and Sensitivity Analysis (DRGEPSA)

method [27] in combination with manual path analysis. A comprehensive validation of the different versions of skeletal

mechanisms and a sensitivity analysis of the chemical mechanisms on the supersonic combustion characteristics would

be beneficial for improving the credibility of supersonic combustion modelings.

    This study will validate the fidelity of the skeletal kerosene mechanisms in a three-level framework. The

mechanisms will be applied to a realistic supersonic combustion modeling to reveal the influence of chemical

mechanisms on the flow, mixing and combustion characteristics. Firstly, a wide range of basic kinetic properties based

on ideal 0-D or 1-D (one-dimensional) flow cases will be evaluated. Then the predictions of time-averaged flow fields

in the realistic combustor will be compared, together with the analysis on efficiency indices. The predictions of

intermediate species and turbulence-chemistry interaction (TCI) modes will be evaluated as the third level of fidelity

validation.

II.   Base-level fidelity validation

    As proposed in [28], the fidelity validation of the mechanisms can be divided into three levels. In the current

implementation of the DRGEPSA method, only a single property target, e.g., either the ignition delay or the laminar

flame speed is selected to match a predefined error threshold. As the replenishment, more property targets that cover

the essential requirements for the mechanism application will be evaluated in the base level of fidelity validation,

which considers little the flow effect. Through applying the mechanism into reacting flow modelings, the second level

of fidelity validation evaluates the accuracy in the predictions of time-averaged or statistical flow quantities based on

the experimental measurements or those predicted by the original mechanism. Such comparisons of steady quantities

require the heat source/sink to be accurately imposed into the flow. The accurate prediction of transient turbulent

combustion processes (e.g., ignition/extinction and flame stabilization) is important for many combustor designs,

hereby the accurate predictions of intermediate species and TCI modes are the focuses of the third level of fidelity

validation.

    The mechanism reduction for kerosene is conducted through a trial and error procedure based on the DRGEPSA

method [27]. The target species are chosen as those should be retained during the reduction or the key species. As a

general rule of thumb, at least the fuel and oxidizer species, and the final products (e.g., H_2O and CO_2) should be listed as the target species, as this study does. Note that usually the more target species are added, the larger the final mechanism size will be. After selecting target species for the mechanism reduction, a graph search in the network composed of interconnecting element reactions in the mechanism is performed to build the dependency paths for all the target species. Direct interaction coefficients (DICs) are calculated between adjacent species along each reaction path. Path interaction coefficient (PIC) is calculated as the product of intermediate DICs and the maximum PIC is defined as the overall interaction coefficient (OIC). Since OIC distinguishes the relative importance of the examined species to the target species, those examined species with OICs below a specified OIC threshold ε_{OIC} are considered to be unimportant species and will be removed. The ε_{OIC} will be automatically adjusted until a maximum allowed deviation is reached between the ignition delays predicted by the skeletal and the detailed mechanisms.

Figure 1 shows the variations of mechanism size and ignition delay error with the ε_{OIC} in the DRGEP (Directed Relation Graph with Error Propagation) reduction stage. Generally, increasing the threshold, a smaller skeletal mechanism can be obtained, but the ignition delay error will increase. The species number quickly drops to below 200 from the original 2185, but an asymptotic behavior appears when further increasing ε_{OIC} and the smallest mechanism size obtained by DRGEP is around 50. The ignition delay error shows a zig-zag rise with the increasing of ε_{OIC}. The OIC only measures the relative importance among the reaction paths connecting the target species, and it does not distinguish the positive or negative contribution of the current reaction path on the ignition delay. For example, some reaction paths may have a negative contribution to the ignition delay, i.e., increasing the path fluxes of those reaction paths will lead to a lower temperature (less heat production), thus eliminating such reaction paths will conversely shorten the ignition delay. This explains the zig-zag rise. However, since increasing the OIC threshold will remove more reaction paths and the corresponding species, the general trend is still to deviate the prediction of ignition delay from the real one predicted by the original mechanism. Continuing to increase the OIC threshold to $\varepsilon_{OIC} = 0.16$, the ignition delay predicted by the skeletal mechanism ($\tau_{Ig,skeletal}$) will derivate from the real one ($\tau_{Ig,detailed}$) with a error up to 100%, which means that $(\tau_{Ig,skeletal} - \tau_{Ig,detailed})/\tau_{Ig,detailed} = 100\%$.
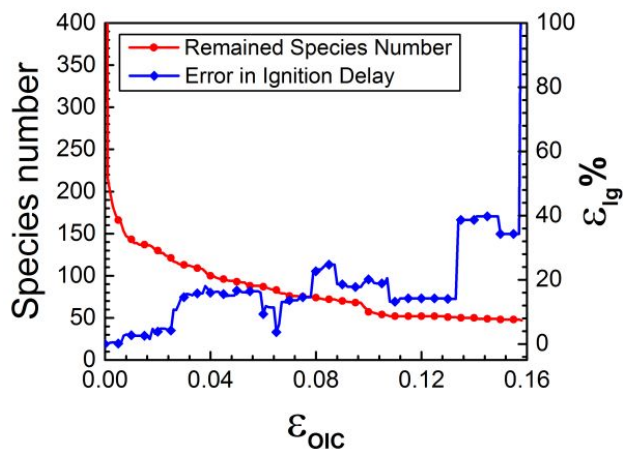
Figure 1. Dependence of mechanism size and ignition delay error on OIC threshold

As the base level of fidelity validations, some preliminary results predicted by the five skeletal mechanisms are shown in Figures 2. Except for the laminar fame speed, the kinetic properties are compared under 1200-2400 K and 1 bar for the premixed mixture at a unity equivalence ratio. Generally, the adiabatic flame temperature and total heat release are accurately predicted by the five skeletal mechanisms compared with the detailed one. Heat release is especially important for enclosure combustion modelings, e.g., combustors, as it determines the pressure rise ratio and even the wave structures.

The ignition delays predicted by the skeletal mechanisms are all in good agreements with the detailed one. Here, the ignition is registered when a specified temperature rise (400 K in this study) has occurred. The 89s mechanism shows the best predictive accuracy since its reaction paths are retained in maximum. The predictions by the 28s and 48s are generally good over the full temperature range. The prediction by the 39s deviates at low temperatures below 1300 K, while the prediction by the smallest 19s mechanism deviates mainly in a middle-temperature range from 1500 to 2000 K.

The laminar flame speeds are compared under 1 bar for the premixed mixture with equivalence ratios from 0.7 to 1.5 and unburnt temperature of 473 K. It is surprising that the laminar flame speed is well predicted by the smaller 39s, 28s, and 19s mechanisms, while larger underpredictions incurred by using the 89s and 48s mechanisms. The laminar flame speed by the 89s mechanism is only slightly underpredicted for equivalence ratios from $\Phi=0.8$ to 1.1. The prediction by the 48s mechanism underestimates the laminar flame speed significantly in the full equivalence ratio range. The laminar flame speed is calculated by solving a set of 1-D governing differential equations for continuity, species, and energy that describes the freely propagating flame dynamics. Unlike the 0-D homogeneous

reactor, the chemical kinetics and transport processes are modeled together in the flame speed simulations. The laminar flame speed is determined not only by the overall reaction rate but also by the thermal diffusivity of selected species. The DRGEPSA reduction process retains species only to ensure that the ignition delay is accurate. For one instance, the 48s and the 19s mechanisms describe the mixtures consisting of different species, whose diffusivity difference may affect the laminar flame speed. In calculating the laminar flame speed, the mixture-averaged diffusivities based on realistic transport database for different species are used, but in the combustor modeling usually constant Prandtl and Schmidt numbers are used to derive the thermal and mass diffusivities from viscosity. From this point of view, the laminar flame speed comparison only has a reference meaning. Indeed the turbulent flame speed is more dependent on the turbulence intensity rather than the kinetic properties of the mixture. That is the reason why the application of the skeletal mechanisms in a realistic case should be conducted to validate their fidelity further. The flame thickness (l_F) can be approximated by the preheat zone thickness as $l_F = k/(\rho C_p S_L)$, where k is the thermal conductivity of unburnt mixture, ρ is the density of unburnt mixthe ture, and C_p is the specific heat of the unburnt mixture, S_L is the laminar flame speed. The flame reactive layer is estimated to be 50-100 μm wide, while the filter size usually remains about 1 mm [29]. As seen, the flame thickness is typically thinner than the grid size, and a significant part of the flame wrinkling induced by the turbulence cannot be resolved by the LES modeling. Therefore, dedicated models for turbulence/flame interactions are needed.

The 89s mechanism predicts the closest time-evolution behaviors for temperature and heat release at an initial temperature of 2400 K. The other skeletal mechanisms overall overestimate the temperature and total heat release, but the discrepancies diminish gradually as approaching the chemical equilibrium status. The predictions of OH concentrations by the 89s mechanism and the detailed mechanism (also referred to as the 89s/48s/38s/28s/19s/detailed predictions for short in the following) are highly coincided, while the OH predictions by the other skeletal mechanisms are underpredicted in the rising stage and then all approach the same in the equilibrium stage. For CH_2O, the 89s mechanism again predicts an almost identical profile with the detailed mechanism, probably because the reaction paths are retained more completely. The other skeletal mechanisms overestimate the mass fraction of CH_2O, especially a large deviation is observed in the prediction by the 19s mechanism. For CO, the 89s and 48s mechanisms predict the closest profiles with the detailed prediction. The 19s and 28s mechanisms overestimate the mass fraction of CO, while the 39s mechanism underpredicts it. Similarly, the 89s again predicts the closest C_2H_4 profile with the detailed prediction. The 28s and 48s mechanisms overestimate the mass fraction of C_2H_4, while the 19s and 39s mechanisms

underpredict it. The peak locations in the C_2H_4 and CH_2O profile are both postponed in the predictions by the 19s

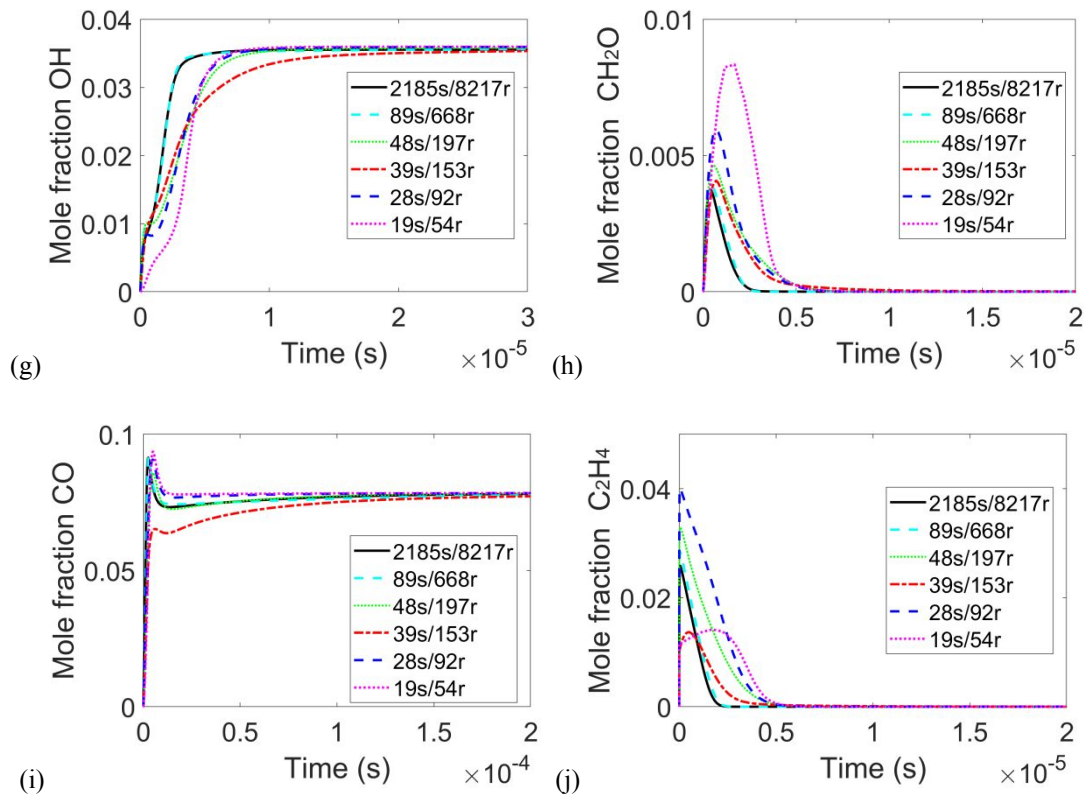mechanism.

(a) (b) (c) (d) (e) (f)
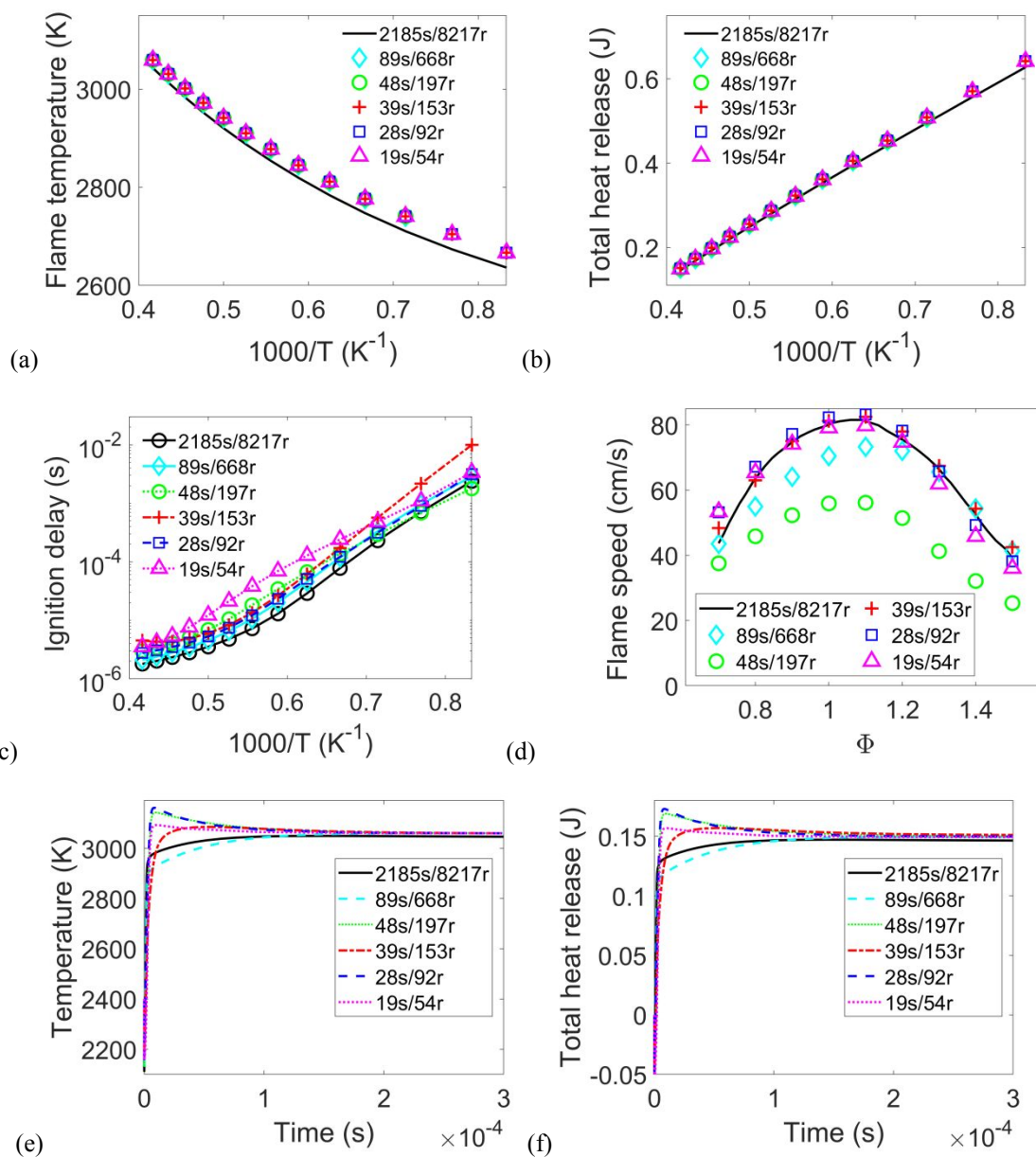
Figure 2. Kinetic property comparisons between different mechanisms for (a) flame temperature, (b) total heat release, (c) ignition delay in logarithmic ordinate, (d) laminar flame speed, time evolutions of (e) temperature, (f) heat release, (g) OH mole fraction, (h) CH$_2$O mole fraction, (i) CO mole fraction, and (j) C$_2$H$_4$ mole fraction

III.   Numerical detail and case setup

A. Governing equations and the AstroFoam solver

The unsteady and 3-D Favre-averaged compressible Navier-Stokes equations are solved for multi-component reactive gas mixtures, which are represented by a set of conservative variables ($\bar{\rho}$, $\tilde{u}_i$, $\tilde{H}_t$, $\tilde{Y}_\alpha$),

$$\frac{\partial \bar{\rho}}{\partial t} + \frac{\partial \bar{\rho}\tilde{u}_j}{\partial x_j} = 0 \tag{1}$$

$$\frac{\partial \bar{\rho}\tilde{u}_i}{\partial t} + \frac{\partial \bar{\rho}\tilde{u}_j\tilde{u}_i}{\partial x_j} + \frac{\partial \bar{p}}{\partial x_i} - \frac{\partial \tilde{\tau}_{ij}}{\partial x_j} = -\frac{\partial \tau_{ij}}{\partial x_j} \tag{2}$$

$$\frac{\partial \bar{\rho}\tilde{H}_t}{\partial t} + \frac{\partial \bar{\rho}\tilde{u}_j\tilde{H}_t}{\partial x_j} - \frac{\partial}{\partial x_j}\left(\bar{\rho}D_T\frac{\partial \tilde{H}_t}{\partial x_j} + \sum_{\alpha=1}^{L}\bar{\rho}D_\alpha\frac{\partial \tilde{Y}_\alpha}{\partial x_j}\tilde{H}_\alpha\right) - \frac{\partial \bar{p}}{\partial t} - \frac{\partial \tilde{u}_j\tilde{\tau}_{ij}}{\partial x_j} = -\frac{\partial \Psi_{T,j}}{\partial x_j} \tag{3}$$

$$\frac{\partial \bar{\rho}\tilde{Y}_\alpha}{\partial t} + \frac{\partial \bar{\rho}\tilde{u}_j\tilde{Y}_\alpha}{\partial x_j} - \frac{\partial}{\partial x_j}\left(\bar{\rho}D_\alpha\frac{\partial \tilde{Y}_\alpha}{\partial x_j}\right) = -\frac{\partial \Psi_{\alpha,j}}{\partial x_j} + \overline{\omega}_\alpha \tag{4}$$

$$\overline{p} = \overline{\rho}R\tilde{T} \tag{5}$$

$$\tilde{H}_t = \tilde{H}^0 + \int_0^T C_p dT + \frac{1}{2}\tilde{u}_i\tilde{u}_i \tag{6}$$

Here the bar "-" and the tilde "~" represent averaged- or Favre-averaged quantities respectively, t denotes the time, x_i is the Cartesian coordinate in direction i, $\overline{\rho}$ is the density, $\tilde{u}_i$ is the velocity component in x_i direction (spatial dimension i = 1, 2, 3), $\overline{p}$ is the pressure, $\tilde{\tau}_{ij}$ is the viscous stress tensor, $\tilde{H}_t = \tilde{H} + 0.5\tilde{u}_i^2$ is the total absolute enthalpy obtained as the sum of the absolute enthalpy $\tilde{H}$ and the resolved kinetic energy, $\tilde{H}^0$ is the formation enthalpy, q_i is the heat flux vector in the ith direction, $\tilde{Y}_\alpha$ is the mass fraction of species α ($\alpha = 1$, ..., L, L is the total species number), the specific heat C_p is a function of species concentrations and temperature, $\overline{\omega}_\alpha$ is the averaged mass production rate of chemical species α in the unit of $kg \cdot m^{-3} \cdot s^{-1}$, D_α is mixture-averaged mass diffusivity of species α, D_T is the thermal diffusivity, $\tilde{T}$ is the temperature, $R = R_u/W$ is the gas constant, $R_u = 8.314\, J \cdot mol^{-1} \cdot K^{-1}$ is the universal gas constant, $W = \left(\sum_{k=1}^{N} Y_\alpha/W_\alpha\right)^{-1}$ is the molar weight of the multicomponent mixture. The thermodiffusion (Soret effect), barodiffusion and mass-driven diffusion of heat (Dufour effect) are all ignored in Eq. (3)-(4).

The Reynolds stresses (τ_{ij}) and turbulent fluxes ($\Psi_{T,j}$ and $\Psi_{\alpha,j}$) in Equation (1)-(6) are unclosed and require specific modeling. The Reynolds stress, defined as $\tau_{ij} = \overline{\rho}\left(\widetilde{u_i u_j} - \tilde{u}_i\tilde{u}_j\right)$, is modeled by Boussinesq eddy viscosity hypothesis. The turbulent enthalpy flux term $\Psi_{T,j} = \overline{\rho}\left(\widetilde{u_j H_t} - \tilde{u}_j\tilde{H}_t\right)$ is modeled by the gradient diffusion assumption with a unity turbulent Prandtl number Pr_t. The turbulent species diffusion term $\Psi_{\alpha,j} = \overline{\rho}\left(\widetilde{u_j Y_\alpha} - \tilde{u}_j\tilde{Y}_\alpha\right)$ is also modeled using the gradient diffusion assumption with a unity turbulent Schmidt number Sc_t.

Improved Delayed Detached Eddy Simulation (IDDES) [30] is employed to model the combustor with the background RANS model is the one-equation Spalart-Allmaras (S-A) model [31]. The Favre-filtered or Favre-averaged Navier–Stokes equations including transport equations for individual species and absolute enthalpy are solved in a uniform framework by equally treating the turbulent viscosity in the RANS (Reynolds-averaged Navier-Stokes) mode and the subgrid-scale (SGS) viscosity in the LES (Large Eddy Simulation) mode. The numerical treatments in resolving Eq. (1)-(6) are the same for any turbulence models, and the switch between RANS and LES is determined by which turbulence model the eddy viscosity is calculated by.

The thermodynamic and transport properties of the gas mixture, such as the absolute enthalpy, specific heat, viscosity, thermal and mass diffusivities are calculated using the chemical kinetics package CHEMKIN-II [32] based on

the JANAF thermophysical table and a CHEMKIN-format transport database. The viscosity, specific heat and conductivity are all independent of pressure but only depend on temperature. The mixture-averaged viscosity and thermal conductivity are calculated using the modified Wilke's law [33] and the combination averaging respectively. The mixture thermal diffusivity is then calculated based on the conductive and specific heat. Mixture-averaged mass diffusivities are used, and the mass conservation is achieved by setting the nitrogen as inert gas, whose mass fraction is computed simply by subtracting the sum of the remaining mass fractions from unity.

PaSR (Partially Stirred Reactor) model [34] is used to estimate the turbulent reaction rate $\overline{\omega}_\alpha$, which is related to the chemical reaction rate (ω_α) by a function of the characteristic time scales of chemistry (τ_c) and micro-mixing (τ_{mix}) as,

$$\overline{\omega}_\alpha = \frac{\tau_c}{\tau_c + \tau_{mix}} \omega_\alpha \tag{7}$$

In the above equation, τ_c is the chemical time scale, τ_{mix} is the micro-mixing time scale, and ω_α is the integral reaction rate over the current integration time step calculated from the Arrhenius law,

$$\omega_\alpha = \sum_{\beta=1}^{M} \omega_{\alpha,\beta} = \sum_{\beta=1}^{M} W_\alpha\left(v''_{\alpha,\beta} - v'_{\alpha,\beta}\right)\left(k_{f,\beta}\prod_{\alpha=1}^{L}[c_\alpha]^{v'_{\alpha,\beta}} - k_{r,\beta}\prod_{\alpha=1}^{L}[c_\alpha]^{v''_{\alpha,\beta}}\right) \tag{8}$$

where $v''_{\alpha,\beta}$ and $k_{f,\beta}$ are respectively the forward stoichiometric coefficient and the forward rate constant of the βth-elementary reaction, $v'_{\alpha,\beta}$ and $k_{r,\beta}$ are their reverse counterparts, c_α is the molar concentration of species α, L and M are respectively the total species and reaction numbers. To speed up the direct integration (DI) of the stiff chemistry, In Situ Adaptive Tabulation (ISAT) method [35] is used to calculate ω_α. The micro-mixing time scale is calculated as the geometric mean of the Kolmogorov time scale (τ_k) and the subgrid time scale (τ_Δ). $\tau_{mix} = \sqrt{\tau_k \tau_\Delta}$. Here $\tau_\Delta = k_t/\epsilon = (v_t/C_\mu \epsilon)^{1/2}$, where k_t is the unresolved turbulent kinetic energy on the subgrid scale and ϵ is its dissipation rate, v_t is the turbulent viscosity v_t, $C_\mu = 0.09$. Then

$$\tau_{mix} = \frac{1}{C_\mu^{1/2}}\left(\frac{\sqrt{v \cdot v_t}}{\epsilon}\right)^{1/2} \tag{9}$$

k_t and ϵ are estimated from their relations with the turbulent viscosity v_t, i.e. $k_t = \left(v_t/(c_k d_{IDDES})\right)^2$ and $\epsilon = 2v_{eff}|\tilde{S}_{ij}|^2$, where d_{IDDES} is the length scale in the IDDES framework, $v_{eff} = v_t + v$, $\tilde{S}_{ij}$ is the computable strain-rate tensor of the resolved scales, and $c_k = 0.07$. The characteristic chemical time scale is calculated as the ratio of the summation

of species concentrations to that of reaction rates $\tau_c = \sum c_\alpha / \max\left(\sum(\omega_\alpha^+ / W_\alpha), \varepsilon\right)$, with ε a small quantity to avoid a zero division. The forward production rates are calculated by only considering the forward reactions and neglecting all their reverse counterparts.

The supersonic combustion modelings are performed by the compressible reacting flow solver AstroFoam, which is developed on the basis of the compressible flow solver rhoCentralFoam [36] distributed with the finite-volume (FV) unstructured CFD package OpenFOAM V3.0.1 [37]. The OpenFOAM CFD package has been coupled with CHEMKIN II chemistry solving package [32] to calculate the multi-component thermophysical and transport properties, as well as SUPERTRAPP V3.1 package [38] to calculate the thermophysical properties of pure kerosene at the fuel inlets. The AstroFoam together with the original rhoCentralFoam solver was firstly validated for various frozen flows, including the canonical shock tube problem, forward step flow, hypersonic flow over a biconic, and supersonic jets [36, 39-43]. The solver has been applied to various scramjet combustor cases [25, 26, 28, 44] to examine its accuracy and robustness in the modeling of complex supersonic combustion.

The nonlinear inviscid convective fluxes in AstroFoam inherited from rhoCentralFoam are evaluated by the semi-discrete central Kurganov-Tadmor (KT) scheme [45]. The face values are interpolated by the third-order scale-selective discretization (SSD) scheme [46]. The temporal integration is advanced by the second-order Crank-Nicolson scheme.

B. Computational domain and boundary conditions

The test case is a round-to-elliptical shape-transition (RdEST) supersonic combustor operated under a flight Mach number of 6.5 and a global fuel equivalence ratio of 0.8. The tests are conducted in a continuous-flow supersonic combustion test facility. Liquid kerosene heated to supercritical status by an electric ceramic heater is delivered to the test article. The scramjet combustors are composed of three sections: a 600-mm-long isolator section with a slight 0.7° divergence angle, an 800-mm-long burner section, and a 600-mm-long expander section with a large 4° divergence angle. Static pressure is measured by Motorola MPX2200 pressure transducers along the inner wall of the combustor assembly all with 50 mm intervals. For more details of the experimental tests, the readers can refer to [26].

The computational domain consists of the isolator, burner and expander sections. The unstructured mesh is generated by the Immersed Boundary (IB) CutCell method (also called Cartesian grid method) [47], where the background Cartesian cells across the immersed boundary are truncated to create new cells with a triangulated surface conforming to the shape of the complex surface. No special treatment is required during the finite-volume discretization of the flow equations in the cells cut by the immersed boundary surface, and the local mass and

momentum conservation are satisfied by simply treating the cutting triangulated surface as a boundary. The CutCell

method can produce high-quality uniform hexahedral grid cells for most of the domain and tetrahedron, wedge or

pyramid cells filled only in large-curvature regions, e.g., those near the borders or corners. As shown in Figure 3, the

whole domain is meshed firstly with a uniform cell size of 1 mm, which is then adaptively refined based on local

curvatures and size functions. The cell size around the fuel injectors is progressively refined to 1/16 of the internal

cell size, i.e., 62.5 μm, which is comparable to the local Kolmogorov scale of 50 μm. For the boundary layer, the

inflation layer comprises of 23 prism sublayers has an average thickness of 2 mm and the last prism in the logarithmic

layer. The initial prism layer height is 5 μm, which corresponds to a non-dimensional wall distance $y^+\sim o(1)$ on all the

wall surfaces for the examined combustor flows. An extension of y^+-insensitive wall treatment is made to the S-A

model through calculating the wall shear stress according to the log-law. The total cell number is 82.39 million. Grid

quality analysis shows that 99.3% of the volume is meshed by hexahedral cells, 94.1% of the volume has a skewness

smaller than 0.1, and 98.4% of the volume has an orthogonal quality higher than 0.9. The coordinate origin is located

at the center of the isolator inlet, with x denotes the streamwise direction that is normal to the inlet plane. To examine

of the sensitivity of the results on the mesh resolution, additional four mesh sets, respectively with 33.28 million,

45.91 million, 55.35 million and 135.60 million cells were tests. The mesh is refined or coarsened through adjusting

the maximum grid size by a step of 0.2 mm, which limits the mesh resolution in most of the domain volume (>98%)

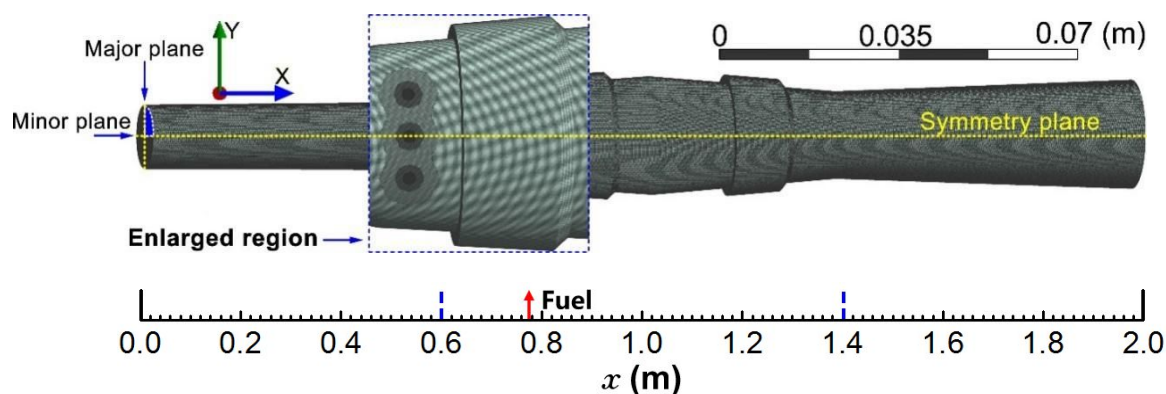except around the fuel injectors.

Figure 3. Mesh distribution in the full-scale domain

Fixed pressure, temperature, velocity, and vitiated air compositions are imposed on the isolator inlet and the fuel

inlets according to those listed in Table 1. The principle of extended corresponding states (ECS) [48] for RP-3 kerosene

is used to calculate the fuel injection velocity from the mass flow rate since the compressibility of supercritical RP-3

cannot be described by the ideal gas equation. The ECS method is also applied to the fuel jet immediately out of the

jet portholes, which corresponds to the mixture with a fuel mole concentration larger than 30%. After the dilution of

the fuel jet by the air crossflow, the ideal gas law becomes applicable. A RANS type turbulent inlet boundary condition

is specified on the isolator inlet by fixing the turbulence viscosity as $\nu_t/\nu = 1$. The wall temperature is specified as a

linear variation from 500 K at the isolator inlet to 1200 K at the expander outlet to roughly mimic the wall extinction

effect. Open boundary condition is applied to the expander outlet, where zero gradient is used for outflow and the

vitiated air flow conditions are specified for backflow values.

The parallel computations are performed at the national supercomputer center in Tianjin (TH-1) using 280 CPU

cores (Intel(R) Xeon(R) CPU E5-2690v4 with the base frequency of 2.60GHz). The time step is limited both by a

maximum Courant number of 0.3 and a user-specified maximum time step of 5×10^{-8} s, which is roughly 1/10th

~1/20th of the chemical time scale. The flush through time (FTT) defined based on the length of the combustor flow-

path length (2 m) and the inlet flow speed of the vitiated air crossflow (1472 m/s) is $1.33 \times 10^{-3}\ s$. Each modeling

case costs about 40×24 hours on their assigned core numbers to ensure at least 4 FTTs ($\approx$ 5 ms) for data sampling

and statistics.

Table 1. Test case configurations

Vitiated air crossflow							RP-3 jet			
$P_{t,\ air}$	$T_{t,\ air}$	$\dot{m}_{air}$	Ma	N_2	O_2	H_2O	$P_{t,\ f}$	$T_{t,\ f}$	$\dot{m}_{fuel}$	Φ
MPa	K	kg/s			mol/mol		MPa	K	kg/s	
13.66	1581.7	3.5789	3.0	60.5%	21.7%	17.8%	5.77	784	0.2181	0.8

IV.   Results and discussion

Figure 4 (a) shows the wall pressure predictions by the five different mesh sets from coarse to fine respectively

with 33.28, 45.91, 55.35, 82.39 and 135.60 million cells. The pressure is sampled on the intersection line of the inner

wall and the major symmetry plane. The chemistry modeling is based on the 19s mechanisms. The differences between

the predictions are visually ignorable. Figure 4 (a) shows the log-log scale plot of the variation of the relative errors

with the nominal grid size. The mean and maximum errors are calculated relative to the finest mean pressure prediction

at the cost of 135.60 million cells. Since the hexahedral cells with the specified maximum grid size fill more than 98%

of the domain volume, the maximum grid size is used as the nominal grid size. Both the mean and maximum errors

decrease roughly linearly in the logarithmic plot as the grid is refined. The mean relative errors decrease from 2.78%,

2.30%, 1.63% to 1.43%, while the maximum relative errors decrease from 11.05%, 9.79%, 7.12% to 7.03%. It is

expected that further refining the mesh, the predictions would only deviate from the finest result by no more than 2%

and 8% in the mean and maximum errors. As a compromise between the accuracy and the cost, the results based on

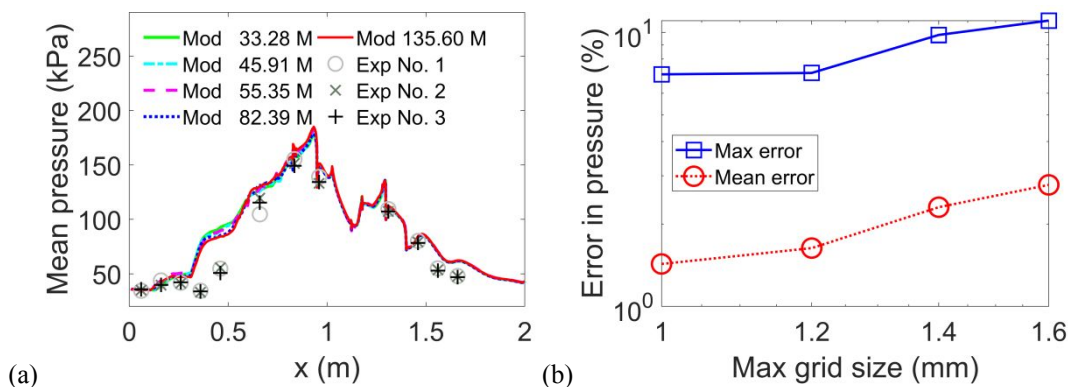the 82.39-million mesh are analyzed in the following analysis.

(a)   (b)

Figure 4. (a) Mean pressure predicted by different mesh resolutions, (b) convergence of relative errors

Figure 5 shows the time-averaged pressure, temperature, Mach number and heat release rate along the streamwise

direction predicted by the four mechanisms. The 89s mechanism is not used in the flow modeling as chemical

mechanisms with species number over 50 is too computational-expensive for finite-rate LES modelings under the

current computational technology. The temperature and Mach number are averaged on each cross-section at different

streamwise locations to compare their streamwise variations. For example, the mean temperature $\overline{T}$ at the streamwise

location x is calculated as

$$\overline{T}_x = \frac{1}{n}\sum_n \frac{\int(\rho\vec{u}T)\cdot d\vec{A}}{\int(\rho\vec{u})\cdot d\vec{A}} \tag{10}$$

where n is the number of time sequences, the subscript x denotes the streamwise location, ρ and $\vec{u}$ are respectively the

flow density and velocity, and A is the cross-section area. The positive and negative heat release rate are summed up

over all the cells within each streamwise interval of 1 cm. The wall pressures predicted by different mechanisms are

almost identical and are in general good agreements with the three repeated measurements. The mean temperature

predicted by the 19s mechanism exhibits slight discrepancies at some locations with those predicted by the other

mechanisms, which are else nearly identical. A step-like rise behavior is observed for the mean temperature, which

reaches it maximum at the trailing edge of the downstream cavity and then shows an almost linear decreasing towards

the expander outlet. The mean Mach number profiles predicted by the 19s mechanism is slightly lower with the other

three predictions, which are almost identical. The Mach number depends not only on the flow temperature but also on

the mixture composition, for that it influences the local sound speed. The deviation in the mean Mach number for the

19s prediction is partially attributed to the fact that reduction in the species number to less than 20 significantly changes

the in-situ molecule weight. The predicted supersonic flow by the 19s mechanism mildly chokes to the sonic speed at

the fuel injection section, whereas the other predictions all indicate the scramjet mode. The 28s, 39s, and 48s

mechanisms predict similar peaks in the positive heat release rate, while the 19s mechanism predicts a higher peak.

The more intense heat release in the 19s prediction is the main cause of the mild choke. A secondary peak in the

positive heat release rate can be observed for all the predictions. Another main difference among the predictions lies

in the depth of the troughs right next to the secondary peak, with a descending order from 28s, 39s, 48s to 19s. The

secondary peak shares the same streamwise location with the negative peak of the heat release rate and is an indicator

of the occurrence of ignition reactions. The negative heat release rate is mainly contributed by those pyrolysis reactions

from large fuel molecules into smaller hydrocarbons. Following the pyrolysis, ignition reactions can occur

simultaneously when the temperature is appropriate or favorable ignition exists. In the current case, the ignition

reactions denoted by the secondary positive peak is possibly initiated by the radicals exchange across the symmetry

planes, since no obvious ignition is observed when a quarterly-split domain is applied [26]. Overall speaking, the mean

flow field comparisons show that the predictions by the 19s mechanism show relatively larger deviations with the

predictions by the other three mechanisms, especially for the Mach number. This raises another fact that should be

taken into consideration when reducing a mechanism, that is, the developed mechanism should not only accurately

predict where and how much the heat addition is imposed into the flow, but also the physical properties of the fluid

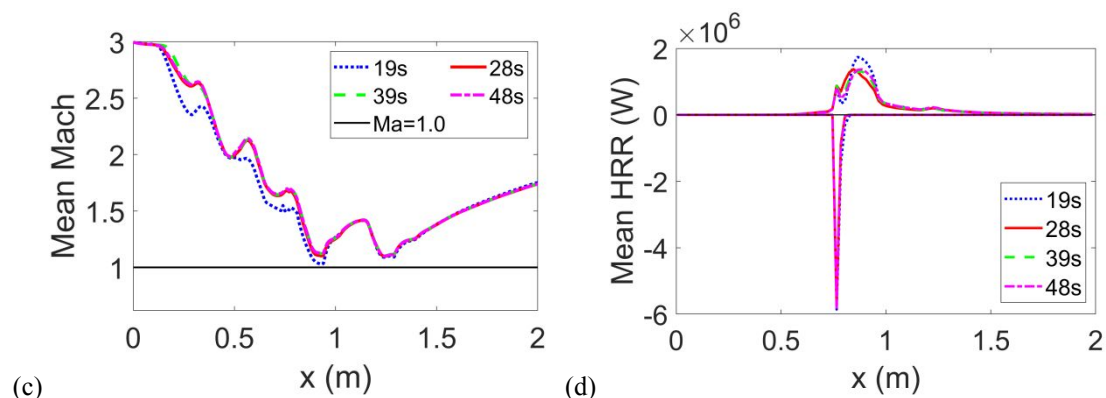should be approximately surrogated by the mechanism constitution.

(a)   (b)

(c)   (d)
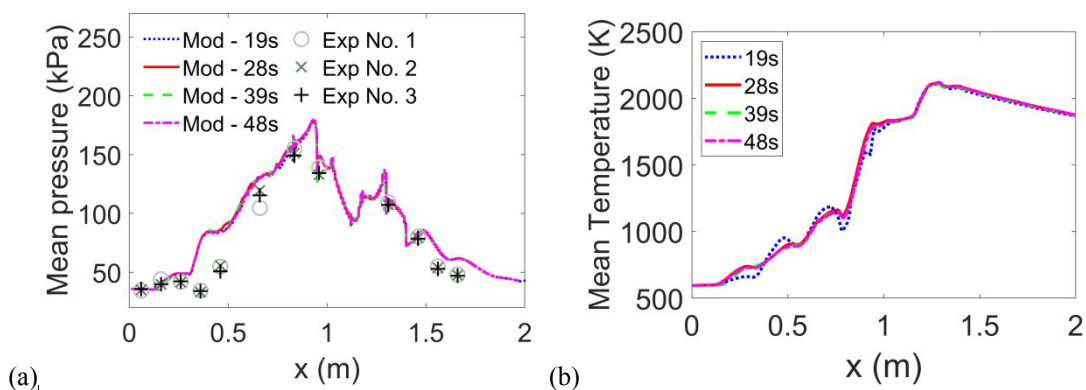
Figure 5. Streamwise variations of mean (a) wall pressure, (b) temperature, (c) Mach number, and (d) heat release rate

Figure 6 compares the mixing efficiency, combustion efficiency and total pressure loss predicted by the different mechanisms following the definitions proposed by Rajasekaran and Babu [49]. Overall, the efficiencies and total pressure loss predicted by the four mechanisms are very similar in both trend and the magnitude. The predictions by the 28s and 48s mechanisms for all the performance indices are almost identical. Compared with them, the 19s mechanism slightly overpredicts while the 39s mechanism slightly underpredicts for most of the streamwise distance, with the deviations all below 5%. Such accuracy is considered acceptable for the performance evaluation of supersonic combustors.

The time-averaged mixing efficiency is calculated as,

$$\eta_{mix} = \frac{1}{n}\sum_n \frac{\dot{m}_{fuel,mixed}}{\dot{m}_{fuel,total}} = \frac{1}{n}\sum_n \frac{\int(\rho\vec{u}Y_{f,react})\cdot d\vec{A}}{\int(\rho\vec{u}Y_f)\cdot d\vec{A}} \tag{11}$$

with

$$Y_{f,react} = \begin{cases} Y_f & Y_f \leq Y_{f,\,st} \\ Y_{f,st}\frac{1-Y_f}{1-Y_{f,\,st}} & Y_f > Y_{f,\,st} \end{cases}$$

where $\dot{m}_{fuel,mixed}$ and $\dot{m}_{fuel,\,total}$ are the mass flow rates of mixed and total fuel, Y_f is the fuel mass fraction, $Y_{f,react}$ is the mass fraction of the fuel that can be reacted, $Y_{f,st}$ is the fuel mass fraction at the stoichiometric condition. To adapt the above mixing efficiency definition for reacting cases, Y_f is derived from the mixture fraction, which is defined based on the element fractions of C, H and O [50]. The mixing efficiency is the highest for the 19s mechanism, and the lowest for the 39s mechanisms, while the 28s and 48s mechanisms predict almost identical profiles. The final mixing efficiencies are 0.91, 0.89, 0.85 and 0.88 respectively for the 19s, 28s, 39s and 48s mechanisms. The fact that the mixing predicted by the 19s mechanism occurs in a slightly more intense way possibly because the reduced

crossflow Mach number allows a higher jet penetration depth since the jet-to-crossflow momentum flux ratio has been actually increased.

Combustion efficiency is calculated as the ratio of the fuel that has been completely converted into the final stable products (e.g., CO_2) [49]. The combustion efficiencies predicted by the four skeletal mechanisms are generally close, and all approach 0.95 at the end of the combustor. The combustion efficiency has a direct relationship with the mixing efficiency, i.e., the quick mixing in the 19s prediction incurs the highest final combustion efficiency while the less intense mixing in the 39s prediction produces the lowest one. This suggests that an early mixing is always favorable for the downstream combustion since only the mixed parcels through a hot zone can be reacted. There is an obvious turning point at x=0.94 m, which corresponds to the trailing edge of the upstream cavity. The turning indicates that the combustion reactions are more intense before the upstream cavity and alleviate since there. The continuous rising of the combustion efficiency suggests that the reactions continuous to covert the intermediate species into the final stable products (H_2O and CO_2). Before the turning point, the 28s mechanism predicts a slightly higher rise in the combustion efficiency, but a more moderate rise after that.

The total pressure loss is defined as the decay ratio of the total pressures at the streamwise location x and at the inlet plane [49]. The streamwise profiles of the total pressure loss predicted by the four mechanisms are similar, especially after the upstream cavity. Before the upstream cavity, the total pressure loss is slightly larger for the 28s mechanism and smaller for the 19s mechanism. The predictions by the 39s and 28s mechanisms are highly close to each other. The final predicted total pressure losses all approach 0.8 at the combustor outlet.
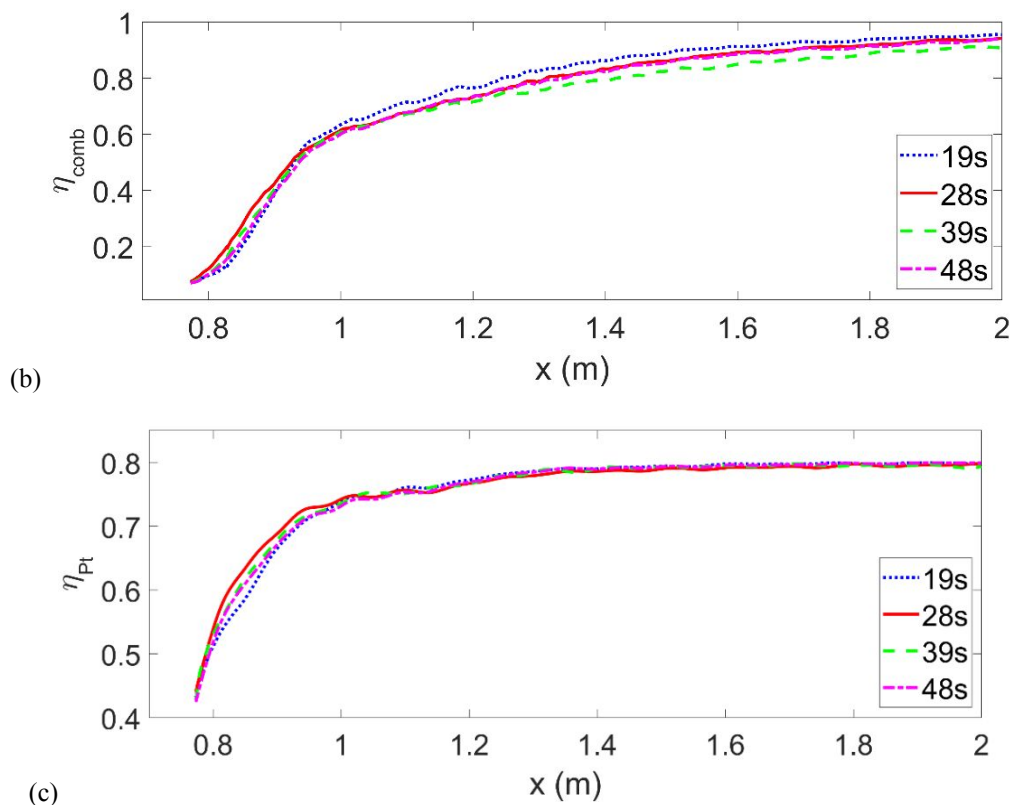

(a)
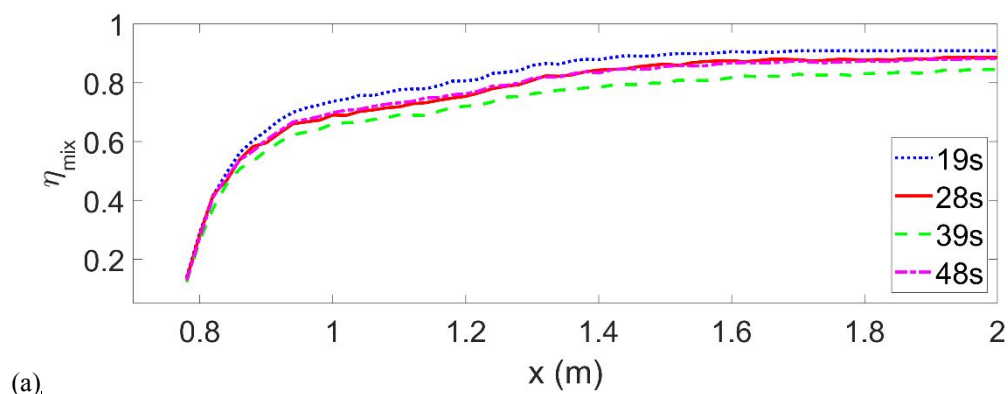
Figure 6. (a) Mixing efficiency, (b) combustion efficiency, and (c) total pressure loss predicted by different skeletal mechanisms

Figure 7 shows the variations of mean mass fractions of intermediate species averaged on each cross-section at different streamwise locations. Four intermediate species are selected based on the reaction path analysis, as they act as critical junctions in the whole path network and have relatively higher temperature sensitivity coefficients. The OH profiles are similar for the 19s, 28s and 48s mechanisms, whereas the 39s mechanism underestimates its mass fraction in the expander section. For CH_2O, two pairs can be divided according to the similarity: the predictions by the 19s and 48s mechanisms, and those by the 28s and 39s mechanisms. As seen, CH_2O is significantly accumulated in the combustion fields predicted by the 19s and 48s mechanisms, implying the balance between its production and consumption fluxes are shifted as the reaction path network varies. The CO mass fractions are similar in the rising stage and diverge after the peak location. The 39s mechanism predicts the highest CO concentration and the 19s predicts the lowest, while the predictions by the 28s and 48s mechanisms are close with each other. As one of the main pyrolysis product of the kerosene surrogate ($NC_{10}H_{22}$, IC_8H_{18}, PCH), the mean mass fraction of C_2H_4 exhibits similarly profiles for the 19s and 39s predictions, and higher peaks in the 28s and 48s predictions. The peaks of the mass fractions of CH_2O, CO and C_2H_4 all occur at around x=0.88 m, which corresponds to the middle of the upstream cavity

and intense heat release rate occurs there as in Figure 5 (d). The primary peak in the OH profile occurs slightly

downstream at x=0.95 m, which corresponds to the trailing edge of the upstream cavity. A secondary peak is observed

in the expander section. The formation of the secondary OH peak is possibly related to the product (e.g., H_2O)

dissociation. The most remarkable observation from the comparisons of intermediate species is the large discrepancies

among different predictions. This is because the path fluxes vary significantly as most of the reaction paths are

removed in the DRGEPSA reduction stage. For example, there are numerous pyrolysis reaction paths from the large-

molecule fuel species to the smaller hydrocarbons (e.g., C_2H_4 and C_3H_6) in the original detailed mechanism, but

usually only one or two are retained after the mechanism reduction. For all the predictions of the intermediate species,

although the magnitudes predicted by different mechanism vary remarkably, but the peak locations and the general

trends agree well with each other. This suggests that the reaction progress along the streamwise distance has been well

predicted, which benefits from the accurately predicted chemical time scales registered as the ignition delay in Figure

2 (c) for all the developed mechanisms. However, the magnitude prediction of intermediate species is unreliable by

using reduced mechanisms. According to the well-known Hess's law, the heat release can be accurately predicted as

long as the production rates of final products are guaranteed in the skeletal mechanisms. This is actually the principle

of most of the reduction methods, i.e., simplifying the reaction paths through the elimination of intermediate species

while emulating the production rates of final products. To obtain a more accurate prediction of any specific

intermediate species, the main reaction paths for them should be retained, possibly through defining them as the target
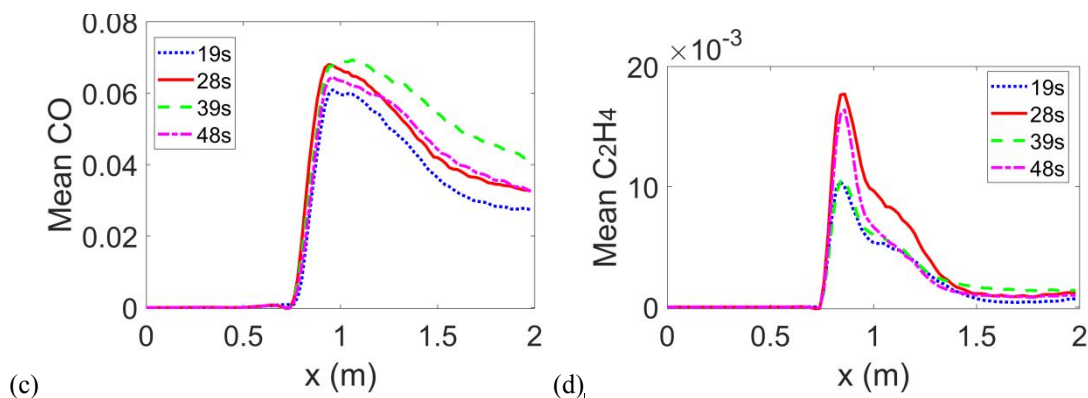
species during the DRGEPSA reduction.

(a)　　　　(b)

(c)   (d)
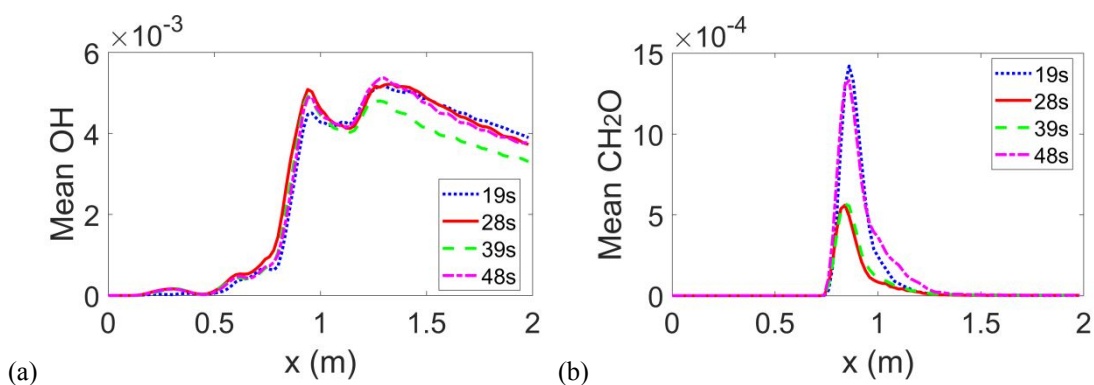
Figure 7. Streamwise variations of mean mass fractions of (a) OH, (b) CH$_2$O, (c) CO, and (d) C$_2$H$_4$

Figure 8 compares the TCI relationship represented by Borghi's diagrams for the different skeletal mechanisms. In calculating Damköhler number Da and Karlovitz number Ka, the Taylor time scale is defined as $\tau_t = (k_{res} + k_t)/\epsilon$ with k_{res} the resolved turbulent kinetic energy, τ_c is calculated as the same as that used in the PaSR model, and the Kolmogorov time scale is defined as $\tau_k = (v/\epsilon)^{1/2}$. The Reynolds number Re is related to Ka and Da as $Re \sim Re' = (\tau_t/\tau_k)^2 = Da^2 \cdot Ka^2$, where a relative Reynolds number (Re') is defined to characterize the relation between Da and Ka. For non-premixed flames, three combustion modes can be divided based on Ka and Da: 1) flamelet mode with $Ka<1$ and $Da>10$, 2) thin reaction zone mode with $1<Ka<100$ (equivalent to $Ka_\delta < 1$) and $Da>10$, 3) slow chemistry mode with $Ka>100$ and $Da<10$. Historical statistics of Da versus Re show that the TCI relationship is also remarkably influenced by the chemical mechanisms used. The flamelet mode maintains a low yet finite existence in the 19s and 28s predictions, but only a trivial existence of around 1% in the 39s and 48s predictions. This indicates that faster reactions possibly occur as the reaction paths are further simplified. From the 19s prediction to the 28s prediction, the percentage of flamelet mode are more than doubled, meanwhile, the percentages of thin reaction zone mode and slow chemistry mode both reduce slightly. The ratio of the three combustion modes are close for the 39s and 48s predictions. The fast chemistry assumption is also approximately valid for the thin reaction zone mode in addition to the flamelet mode. This implies that the fast chemistry assumed flamelet models are inapplicable to around 1/3 of the data points for the 19s and 28s predictions, with the percentage further increases to 38% for the 39s and 48s predictions. As a general rule of thumb, the more complex the reaction paths are, the slower the product formation when coupled with the flow. This is because the transport of individual species may affect the integrity of the reaction paths towards the final products, i.e., a phenomenon of species defect may occur due to the differential diffusion. On the other hand, change in the chemical mechanism influences not only the chemical time scale but also the turbulence characteristics

through redistributing heat release in the flowfield. To gain a deep understanding of the underlying influencing factors

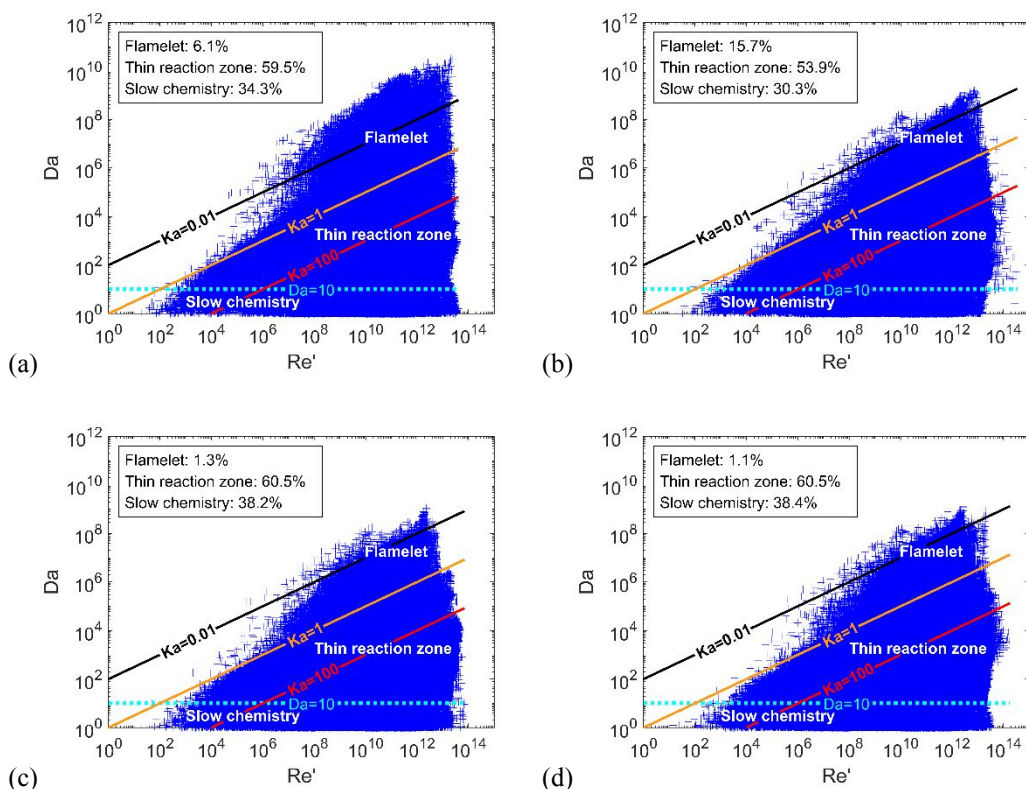for the TCI mode shifting, a high-resolution modeling resolving to the level of flame front is required.

Figure 8. Borghi's diagrams predicted by (a) 19s, (b) 28s, (c) 39s and (d) 48s mechanisms

V.   Conclusions

Five skeletal mechanisms for kerosene, respectively with 89s/668r, 48s/197r, 39s/153r, 28s/92r and 19s/54r were

derived by using the DRGEPSA method from the Dagaut's original mechanism with 2185s/8217r. As a base level of

fidelity validation, the skeletal mechanisms were firstly validated in ideal reactors for typical combustor working

conditions and then applied to model a realistic supersonic combustor. The hybrid RANS/LES IDDES framework

together with the finite-rate PaSR combustion model is applied to model the wall-bounded turbulent reacting flow in

the supersonic combustor based on an unstructured mesh with 82.39 million cells.

Although the mechanism size has been significantly reduced, the key kinetic properties such as adiabatic flame

temperature, heat release rate, ignition delay, and laminar flame speed agree well with the original detailed mechanism.

Generally, the adiabatic flame temperature and total heat release are accurately predicted by the five skeletal

mechanisms compared with the detailed one. The predictions of ignition delay by the 89s, 48s and 28s are good over

the full temperature range, while the 39s prediction deviates at low temperatures (<1300 K) and the prediction by the 19s prediction deviates mainly in a middle-temperature range from 1500 to 2000 K. The laminar flame speed is well predicted by the smaller 39s, 28s, and 19s mechanisms, while larger underpredictions incurred by using the 89s and 48s mechanisms. The decreasing trend of laminar flame speed with the increase of pressure indicates that the kerosene combustion reactions overall exhibit the first-order behavior. The time-evolution profiles of temperature and total heat release are generally similar.

Mean flow fields and efficiency indices are compared. The wall pressures predicted by different mechanisms are almost identical and are in general good agreements with the measurements. The mean temperature predicted by the 19s mechanism exhibits slight discrepancies at some locations with the other predictions, which are else nearly identical. The mean Mach number profile predicted by the 19s mechanism indicates a mild thermal choke, whereas the other predictions all indicate the scramjet mode. The peak positive heat release rate predicted by the 19s mechanism is higher, with the others similar. The 19s mechanism predicts the highest finial mixing efficiency of 0.91, and the 39s mechanism predicts the lowest one of 0.85, while the 28s and 48s mechanisms predict almost identical mixing profiles. The combustion efficiency has a direct relationship with the mixing efficiency, i.e., the quick mixing in the 19s prediction incurs the highest final combustion efficiency while the less intense mixing in the 39s prediction produces the lowest one. The total pressure loss predicted by different mechanisms are similar and all approach 0.8 at the combustor end.

Large discrepancies are observed for the predictions of intermediate species, due to the vast change in the path fluxes among different skeletal mechanisms. From the Borghi's diagrams, the flamelet mode maintains a low yet finite existence in the 19s and 28s predictions, but only a trivial existence of around 1% in the 39s and 48s predictions. The fast chemistry assumed combustion models are inapplicable to around 1/3 of the data points for the 19s and 28s predictions, and the percentage further increases to 38% for the 39s and 48s predictions.

In sum, the 28s mechanism overall shows the best agreements with the detailed mechanism in the base-level fidelity validation. In the second level of fidelity validation, all skeletal mechanisms produce similar mean predictions except that the 19s mechanism shows slightly larger deviations. For the third level of fidelity validation, vast variations exist in the predictions of intermediate species and TCI modes. Because the skeletal or reduced mechanisms are derived under a narrower range of thermochemical conditions, it would be difficult to develop a skeletal/reduced mechanism suitable for all the conditions that the detailed mechanism is designed for. The thermochemical conditions

vary both spatially and temporally in a realistic reacting flow, therefore a more reliable approach would be adaptively

updating the skeletal/reduced mechanisms for different flow regions to describe the local chemistry best and also

minimize the in situ mechanism size.

Acknowledgments

References

1. Lu, T.; Law, C. K., Toward accommodating realistic fuel chemistry in large-scale computations. *Progress in Energy and Combustion Science* **2009,** 35, (2), 192-215.
2. Edwards, T.; Maurice, L. Q., Surrogate Mixtures to Represent Complex Aviation and Rocket Fuels. *Journal of Propulsion and Power* **2001,** 17, (2), 461-466.
3. Dagaut, P.; Karsenty, F.; Dayma, G.; Diévart, P.; Hadj-Ali, K.; Mzé-Ahmed, A.; Braun-Unkhoff, M.; Herzler, J.; Kathrotia, T.; Kick, T.; Naumann, C.; Riedel, U.; Thomas, L., Experimental and detailed kinetic model for the oxidation of a Gas to Liquid (GtL) jet fuel. *Combustion and Flame* **2014,** 161, (3), 835-847.
4. Lindstedt, R. P.; Maurice, L. Q., Detailed Chemical-Kinetic Model for Aviation Fuels. *Journal of Propulsion and Power* **2000,** 16, (2), 187-195.
5. Dagaut, P.; Cathonnet, M., The ignition, oxidation, and combustion of kerosene: A review of experimental and kinetic modeling. *Progress in Energy and Combustion Science* **2006,** 32, (1), 48-92.
6. Dagaut, P., On the kinetics of hydrocarbons oxidation from natural gas to kerosene and diesel fuel. *Physical Chemistry Chemical Physics* **2002,** 4, (11), 2079-2094.
7. Dagaut, P.; Reuillon, M.; Boettner, J.-C.; Cathonnet, M., Kerosene combustion at pressures up to 40 atm: Experimental study and detailed chemical kinetic modeling. *Symposium (International) on Combustion* **1994,** 25, (1), 919-926.
8. Mzé-Ahmed, A.; Dagaut, P.; Hadj-Ali, K.; Dayma, G.; Kick, T.; Herbst, J.; Kathrotia, T.; Braun-Unkhoff, M.; Herzler, J.; Naumann, C.; Riedel, U., Oxidation of a Coal-to-Liquid Synthetic Jet Fuel: Experimental and Chemical Kinetic Modeling Study. *Energy & Fuels* **2012,** 26, (10), 6070-6079.
9. Zeng, W.; Liang, S.; Li, H.-x.; Ma, H.-a., Chemical kinetic simulation of kerosene combustion in an individual flame tube. *Journal of Advanced Research* **2014,** 5, (3), 357-366.
10. Fureby, C.; Chapuis, M.; Fedina, E.; Karl, S., CFD analysis of the HyShot II scramjet combustor. *Proceedings of the Combustion Institute* **2011,** 33, (2), 2399-2405.
11. Cecere, D.; Ingenito, A.; Giacomazzi, E.; Romagnosi, L.; Bruno, C., Hydrogen/air supersonic combustion for future hypersonic vehicles. *International Journal of Hydrogen Energy* **2011,** 36, (18), 11969-11984.
12. Kim, S. H.; Donde, P.; Raman, V.; Lin, K.-C.; Carter, C. In *Large eddy simulation based Studies of Reacting and Non-reacting Transverse Jets in Supersonic Crossflow*, 50th AIAA Aerospace Sciences Meeting including the New Horizons Forum and Aerospace Exposition, Nashville, Tennessee, January 10, 2012; American Institute of Aeronautics and Astronautics: Nashville, Tennessee, 2012.
13. Chaitanya, G.; Jung, C.; Srikant, S.; Suresh, M. In *Large Eddy Simulation of Supersonic Combustion in a Cavity-Strut Flameholder*, 49th AIAA Aerospace Sciences Meeting including the New Horizons Forum and Aerospace Exposition, Orlando, Florida, 4-7 January, 2011; American Institute of Aeronautics and Astronautics: Orlando, Florida, 2011.
14. Sun, M.-b.; Geng, H.; Liang, J.-h.; Wang, Z.-g., Mixing Characteristics in a Supersonic Combustor with Gaseous Fuel Injection Upstream of a Cavity Flameholder. *Flow, Turbulence and Combustion* **2008,** 82, (2), 271-286.
15. Kumaran, K.; Babu, V., Mixing and Combustion Characteristics of Kerosene in a Model Supersonic Combustor. *Journal of Propulsion and Power* **2009,** 25, (3), 583-592.
16. Kumaran, K.; Behera, P. R.; Babu, V., Numerical Investigation of the Supersonic Combustion of Kerosene in a Strut-Based Combustor. *Journal of Propulsion and Power* **2010,** 26, (5), 1084-1091.
17. Zhang, M.; Hu, Z.; He, G.; Liu, P., Large-eddy simulation of kerosene spray combustion in a model scramjet chamber. *Proceedings of the Institution of Mechanical Engineers, Part G: Journal of Aerospace Engineering* **2010,** 224, (9), 949-960.

18. Zhang, M.; Hu, Z.; Luo, K. H.; He, G. In *LES of Kerosene Spray Combustion with Pilot Flame in a Model Dual Mode Ramjet Chamber*, 45th AIAA/ASME/SAE/ASEE Joint Propulsion Conference & Exhibit, Denver, Colorado, 2-5 August, 2009; American Institute of Aeronautics and Astronautics: Denver, Colorado, 2009.

19. Hautman, D. J.; Dryer, F. L.; Schug, K. P.; Glassman, I., A Multiple-step Overall Kinetic Mechanism for the Oxidation of Hydrocarbons. *Combustion Science and Technology* **1981,** 25, (5-6), 219-235.

20. Westbrook, C. K.; Dryer, F. L., Chemical kinetic modeling of hydrocarbon combustion. *Progress in Energy and Combustion Science* **1984,** 10, (1), 1-57.

21. Franzelli, B.; Riber, E.; Sanjosé, M.; Poinsot, T., A two-step chemical scheme for kerosene–air premixed flames. *Combustion and Flame* **2010,** 157, (7), 1364-1373.

22. Choi, J.-Y. In *A quasi global mechanism of kerosene combustion for propulsion applications*, 47th AIAA/ASME/SAE/ASEE Joint Propulsion Conference & Exhibit, San Diego, California, 31 July - 03 August, 2011; San Diego, California, 2011.

23. Yao, W.; Wang, J.; Lu, Y.; Fan, X., Skeletal mechanism generation based on DRGEPSA for Daqing RP-3 aviation kerosene and numerical validation. In *The 7th National Conference on Hypersonic Science and Technology*, Hypersonic Reseach Center CAS: Beijing, 2014; Vol. CSTAM2014-A62-B0044.

24. Yao, W.; Wang, J.; Lu, Y.; Li, X.; Fan, X. In *Full-scale Detached Eddy Simulation of kerosene fueled scramjet combustor based on skeletal mechanism*, 20th AIAA International Space Planes and Hypersonic Systems and Technologies Conference, Glasgow, Scotland, 6-9 July, 2015; Glasgow, Scotland, 2015.

25. Yao, W.; Lu, Y.; Wu, K.; Wang, J.; Fan, X., Modeling analysis of an actively-cooled scramjet combustor under different kerosene/air ratios. *Journal of Propulsion and Power* **2018,** 34, (4), 975-991.

26. Yao, W.; Yuan, Y.; Li, X.; Wang, J.; Wu, K.; Fan, X., Comparative Study of Elliptic and Round Scramjet Combustors Fueled by RP-3. *Journal of Propulsion and Power* **2018,** 34, (3), 72-786.

27. Niemeyer, K. E.; Sung, C.-J.; Raju, M. P., Skeletal mechanism generation for surrogate fuels using directed relation graph with error propagation and sensitivity analysis. *Combustion and Flame* **2010,** 157, (9), 1760-1770.

28. Wu, K.; Yao, W.; Fan, X., Development and Fidelity Evaluation of a Skeletal Ethylene Mechanism under Scramjet-Relevant Conditions. *Energy and Fuels* **2017** 31, (12), 14296-14305.

29. B. Fiorina; Vié, A.; Franzelli, B.; Darabiha, N.; Massot, M.; Dayma, G.; Dagaut, P.; Moureau, V.; Vervisch, L.; Berlemont, A.; Sabelnikov, V.; E. Riber, B. C., Modeling Challenges in Computing Aeronautical Combustion Chamber. *Aerospacelab Journal* **2016,** 11, (AL11-05).

30. Shur, M. L.; Spalart, P. R.; Strelets, M. K.; Travin, A. K., A Hybrid RANS-LES Approach with Delayed-DES and Wall-Modelled LES Capabilities. *International Journal of Heat and Fluid Flow* **2008,** 29, 1638-1649.

31. Spalart, P. R.; Allmaras, S. R., A One-Equation Turbulence Model for Aerodynamic Flows. *La Recherche Aerospatiale* **1994,** 1, 5-21.

32. Kee, R. J.; Rupley, F. M.; Miller, J. A. *Chemkin-II: a fortran chemical kinetics package for the analysis of gas-phase chemical kinetics*; Sandia National Laboratories: Sandia, 1 September, 1989.

33. Bird, R. B.; Stewart, W. E.; Lightfoot, E. N., Viscosity and the Mechanisms of Momentum Transport. In *Transport Phenomena (2nd Edition)*, John Wiley & Sons: New York, 2002; p 27.

34. Golovitchev, V. I.; Nordin, N.; Jarnicki, R.; Chomiak, J. In *3-D Diesel Spray Simulations Using a New Detailed Chemistry Turbulent Combustion Model*, CEC/SAE Spring Fuels & Lubricants Meeting & Exposition, Paris, France, 2000; Paris, France, 2000.

35. Pope, S. B., Computationally efficient implementation of combustion chemistry using in situ adaptive tabulation. *Combustion Theory and Modeling* **1997,** 1, (1), 41-63.

36. Greenshields, C. J.; Weller, H. G.; Gasparini, L.; Reese, J. M., Implementation of semi-discrete, non-staggered central schemes in a colocated, polyhedral, finite volume framework, for high-speed viscous flows. *International Journal for Numerical Methods in Fluids* **2009,** 38, (2), 139-161.

37. Weller, H. G.; Tabor, G.; Jasak, H.; Fureby, C., A Tensorial Approach to CFD using Object Oriented Techniques. *Computers in Physics* **1997,** 12, (6), 620-631.

38. Huber, M. L. *NIST Thermophysical Properties of Hydrocarbon Mixtures Database (SUPERTRAPP) V3.1*; National Institute of Standards and Technology: Boulder, Colorado, February, 2003.

39. Li, X.; Zhou, R.; Yao, W.; Fan, X., Flow characteristic of highly underexpanded jets from various nozzle geometries. *Applied Thermal Engineering* **2017,** 125, 240-253.

40. Li, X.; Fan, E.; Yao, W.; Fan, X., Numerical investigation of characteristic frequency excited highly underexpanded jets. *Aerospace Science and Technology* **2017,** 63, 304-316.

41. Li, X.; Wu, K.; Yao, W.; Fan, X., A Comparative Study of Highly Underexpanded Nitrogen and Hydrogen Jets Using Large Eddy Simulation. *International Journal of Hydrogen Energy* **2015,** 41, (9), 5151-5161.

42. Li, X.; Yao, W.; Fan, X., Large-Eddy Simulation of Time Evolution and Instability of Highly Underexpanded Sonic Jets. *AIAA Journal* **2016,** 54, (10), 3191-3211.

43. Lee, Y.; Yao, W.; Fan, X., Low-dissipative hybrid compressible solver designed for large eddy simulation of supersonic turbulent flows. *AIAA Journal* **2018,** 56, (8), 3086-3096.

44. Wu, K.; Zhang, P.; Yao, W.; Fan, X., Numerical Investigation on Flame Stabilization in DLR Hydrogen Supersonic Combustor with Strut Injection. *Combustion Science and Technology* **2017,** 189, (12), 2154-2179.

45. Kurganov, A.; Tadmor, E., New High-Resolution Central Schemes for Nonlinear Conservation Laws and Convection–Diffusion Equations. *Journal of Computational Physics* **2000,** 160, (1), 241-282.

46. Vuorinen, V.; Larmi, M.; Schlatter, P.; Fuchs, L.; Boersma, B. J., A low-dissipative, scale-selective discretization scheme for the Navier–Stokes equations. *Computers & Fluids* **2012,** 70, 195-205.

47. Clarke, D. K.; Hassan, H. A.; Salas, M. D., Euler calculations for multielement airfoils using Cartesian grids. *AIAA Journal* **1986,** 24, (3), 353-358.

48. Fan, X.; Yu, G., Analysis of thermophysical properties of Daqing RP-3 aviation kerosene. *Journal of Propulsion Technology* **2006,** 27, (2), 187-192.

49. Rajasekaran, A.; Babu, V., Numerical Simulation of Three-Dimensional Reacting Flow in A Model Supersonic Combustor. *Journal of Propulsion and Power* **2006,** 22, (4), 820-827.

50. Bilger, R. W.; Starner, S. H.; Kee, R. J., On reduced mechanisms for methane-air combustion in non-premixed flames. *Combustion and Flame* **1990,** 80, (2), 135-149.